

The published version of this manuscript can be found in Nature Physics:

<http://www.nature.com/nphys/journal/vaop/ncurrent/full/nphys3592.html>

(Advanced online publication)

<http://dx.doi.org/doi:10.1038/nphys3592>

Quantum oscillations of the critical current and high field superconducting proximity in ballistic graphene

M. Ben Shalom¹, M. J. Zhu¹, V. I. Fal'ko², A. Mishchenko¹, A. V. Kretinin¹, K. S. Novoselov¹, C. R. Woods¹, K. Watanabe³, T. Taniguchi³, A. K. Geim¹, J. R. Prance²

¹*School of Physics & Astronomy, University of Manchester, Oxford Road, M13 9PL Manchester, UK*

²*Department of Physics, University of Lancaster, Lancaster, UK*

³*National Institute for Materials Science, 1-1 Namiki, Tsukuba, 305-0044 Japan*

Graphene-based Josephson junctions have attracted significant interest as a novel system to study the proximity effect¹⁻³ due to graphene's unique electronic spectrum and the possibility to tune junction properties by gate voltage⁴⁻¹⁶. Here we describe graphene junctions with the mean free path of several micrometers, low contact resistance and large supercurrents. Such devices exhibit pronounced Fabry-Pérot oscillations not only in the normal-state resistance but also in the critical current. The proximity effect is mostly suppressed in magnetic fields of <10 mT, showing the conventional Fraunhofer pattern. Unexpectedly, some proximity survives even in fields higher than 1 T. Superconducting states randomly appear and disappear as a function of field and carrier concentration, and each of them exhibits a supercurrent carrying capacity close to the universal limit^{17,18} of $e\Delta/h$ where Δ is the superconducting gap, e the electron charge and h Planck's constant. We attribute the high-field Josephson effect to mesoscopic Andreev states that persist near graphene edges. Our work reveals new proximity regimes that can be controlled by quantum confinement and cyclotron motion.

The superconducting proximity effect relies on penetration of Cooper pairs from a superconductor (S) into a normal metal (N) and is most pronounced in systems with transparent SN interfaces and weak scattering so that superconducting correlations penetrate deep inside the normal metal. Despite being one atom thick and having a low density of states, which vanishes at the Dirac point, graphene (G) can exhibit low contact resistance and ballistic transport on a micrometer scale^{19,20} exceeding a distance between superconducting leads by an order of magnitude. These properties combined with the possibility to electrostatically control the carrier density n offer tunable Josephson junctions in a regime that can be referred to as ballistic proximity superconductivity²¹. Despite intense interest in SGS devices³⁻¹⁶ that can show features qualitatively different from the conventional SNS behavior^{2,3}, ballistic graphene Josephson junctions^{15,16} remain little studied.

Our SGS devices are schematically shown in Fig. 1 and described in further detail in Supplementary Section 1. The essential technological difference from the previously studied SGS junctions⁴⁻¹⁴ is the use of graphene encapsulated between boron-nitride crystals^{19,20} as well as a new nanostrip geometry of the contacts. This allows high carrier mobility, low charge inhomogeneity and low contact resistance. More than twenty SGS junctions with the width W between 3 and 8 μm and the length L between 0.15 and 2.5 μm were studied, all exhibiting a finite supercurrent at low temperatures (T), reproducible behaviour and consistent changes with L and W . First, we characterize the devices above the transition temperature $T_c \approx 7$ K of our superconducting contacts. Fig. 1b shows examples of the normal-state resistance R_n as a function of back gate voltage V_g that changes n in graphene. The neutrality point (NP) was found shifted to negative V_g by a few V, with the shift being consistently larger for shorter devices (Supplementary Information). This is due to

electron doping induced by our Nb contacts. For ballistic graphene, such doping is uniform away from the metal interface²². The observed smearing of $R_n(V_g)$ curves near the NP allows an estimate for charge inhomogeneity in the graphene bulk as $\approx 2 \times 10^{10} \text{ cm}^{-2}$. For consistency, data for devices with different L are presented as a function of ΔV_g , the gate voltage counted from the NP.

For positive ΔV_g (electron doping) and $n > 10^{11} \text{ cm}^{-2}$, SGS junctions made from the same graphene crystal and having the same W exhibit the same $R_n(\Delta V_g)$ dependence, independently of L (Fig. 1b). This shows that mean free path is larger than the contact separation and yields carrier mobility $> 300,000 \text{ cm}^2 \text{ V}^{-1} \text{ s}^{-1}$, in agreement with the quality measured for similarly made Hall bar devices. The dashed curve in Fig. 1b indicates the behavior expected in the quantum ballistic limit, $R_Q = (h/e^2)/4N$ where $N = \text{int}(2W/\lambda_F)$ is the number of propagating electron modes, λ_F the Fermi wavelength that depends on $n(\Delta V_g)$ and the factor 4 corresponds to graphene's degeneracy. The difference between R_Q and the experimental curves yields a record low contact resistivity, $\approx 35 \text{ Ohm } \mu\text{m}$. This value corresponds to an angle-averaged transmission probability $Tr \approx 0.8$ (Supplementary Section 2).

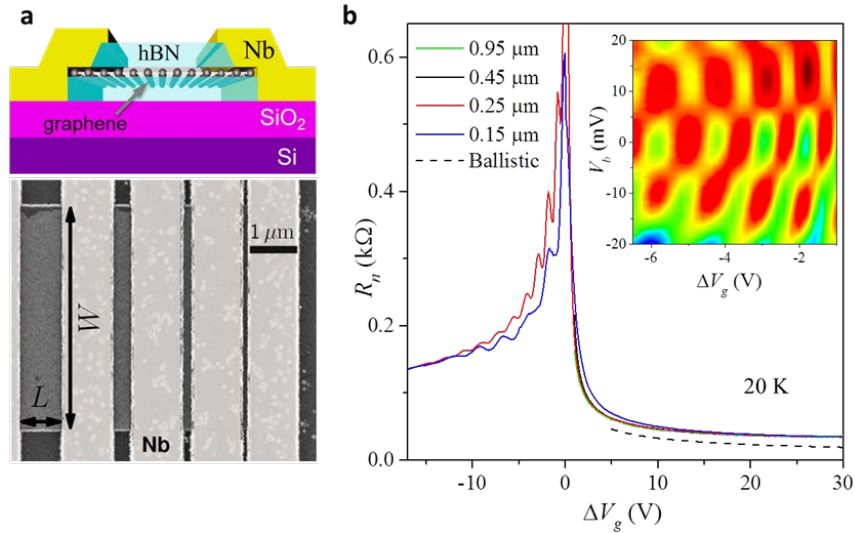


Figure 1 | Ballistic SGS junctions. **a**, Top: Junctions' schematics. Bottom: Electron micrograph of a set of four junctions with different L . A few nm-wide graphene ledge (top drawing) is referred to as a nanostrip contact. **b**, Typical behavior for SGS junctions with different L but for the same set of junctions with $W = 5 \mu\text{m}$. To avoid an obscuring overlap between four oscillating curves, we plot R_n at negative ΔV_g only for the two shortest junctions. For positive $\Delta V_g > 5 \text{ V}$, the four curves overlap within the line width. The dashed curve shows calculated $R_Q(n)$. Inset: Changes in the differential conductance dI/dV ; $L = 0.25 \mu\text{m}$. Color scale: -1 to 1 mS.

For hole doping, R_n becomes significantly higher indicating smaller Tr . This is because pn junctions appear at the Nb contacts and lead to partial reflection of electron waves, which effectively creates a Fabry-Pérot (FP) cavity^{5,23}. The standing waves lead to pronounced oscillations in R_n as a function of both V_g and applied bias V_b (Fig. 1b). The oscillatory behavior indicates that charge carriers can cross the graphene strip several times preserving their monochromaticity and coherence. Some FP oscillations could also be discerned for positive ΔV_g but they were much weaker because of higher Tr . The observed FP behavior in the normal state agrees with the earlier reports^{5,23}. Its details can be modelled accurately if we take into account that the position of pn junctions varies with V_g so that the effective length of the FP interferometer becomes notably shorter than L at low hole doping (Supplementary Section 3).

After characterizing our SGS devices at $T > T_C$, we turn to their superconducting behavior. All of the junctions (including $L = 2.5 \mu\text{m}$) exhibited the fully developed proximity effect. Figures 2a,b show that the critical current I_c remained finite at the NP and rapidly increased with $|\Delta V_g|$, reaching densities $> 5 \mu\text{A}/\mu\text{m}$ for high electron doping and short L , notably larger than I_c previously reported⁴⁻¹⁶. Such high I_c are due to ballistic transport and low contact resistance. Indeed, I_c can theoretically reach a value^{2,24}

$$I_c = \alpha \Delta / e R_n \quad (1)$$

with $\alpha \approx 2.1$. Because in our devices $R_n \approx R_Q = h/4Ne^2$, the equation implies that we approach the quantum limit $I_c \approx (e\Delta/h)4N$ where the supercurrent is determined solely by the number of propagating electronic modes that transfer Cooper pairs between superconducting contacts, and each of the modes has the supercurrent carrying capacity^{3,17} $I_Q \approx e\Delta/h$.

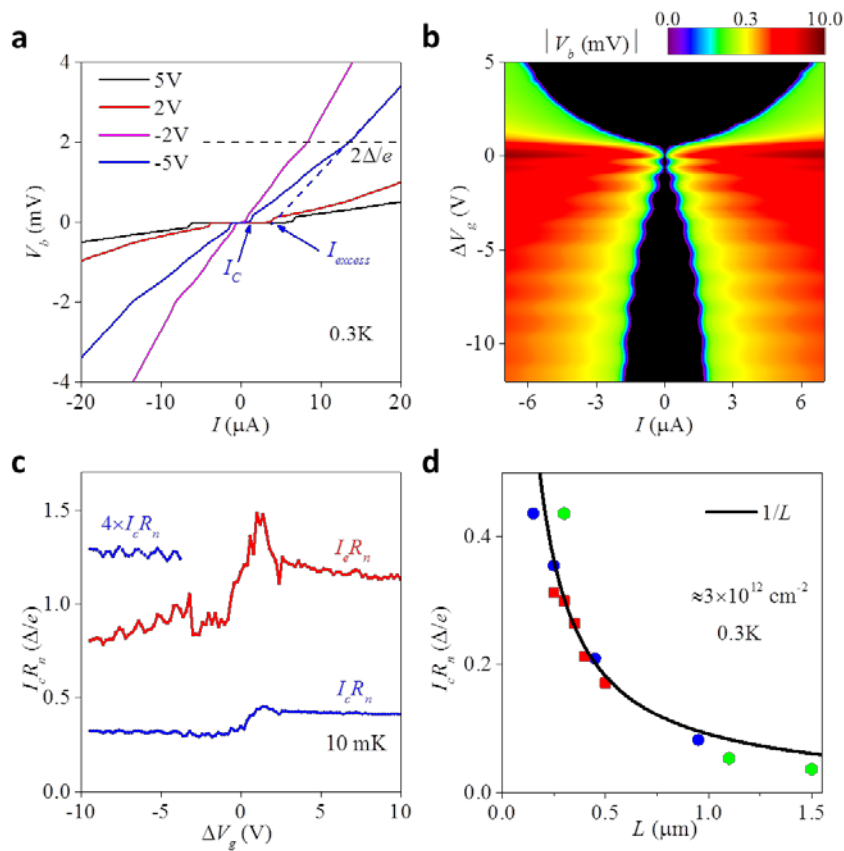


Figure 2] Quantum oscillations in supercurrent. **a**, Examples of I-V characteristics for ballistic SGS junctions in the superconducting state. The data are for the device in Fig. 1 with $L = 0.25 \mu\text{m}$. The arrows explain notions I_c and I_e . **b**, Absolute voltage drop $|V_b|$ across the SGS junction in (a) for a wide range of doping. The black region corresponds to the zero-resistance state, and its edge exhibits clear FP oscillations. **c**, $I_c R_n$ and $I_e R_n$ for a device with $L = 0.3 \mu\text{m}$, $W = 6.5 \mu\text{m}$ and $\Delta \approx 0.8 \text{ meV}$ estimated from its T_C . Each data point is extracted from a trace such as in (a). Inset: Oscillatory part of $I_c R_n$ is magnified. Similar behavior was observed for other devices. **d**, Effect of the junction length on supercurrent for 12 devices with different W . Red symbols - $W = 3 \mu\text{m}$; blue - $5 \mu\text{m}$; green - $6.5 \mu\text{m}$. For each data set, I_c follows the same dependence as $I_c R_n$ because R_n were practically independent of L for the same W . For the two longest devices in (d), the critical current falls below the plotted $1/L$ dependence, probably because of thermal fluctuations (Supplementary Section 4).

Equation (1) suggests that $I_c R_n$ should be a constant. This holds well in our SGS devices away from the NP (Fig. 2c) and indicates that, at low T , external noise, fluctuations and other mechanisms⁴⁻¹⁶ which are dependent on n or R_n do not limit I_c . However, Fig. 2c yields α that is notably smaller than the expected constant in eq. (1). For hole doping, this can be attributed to the presence of pn junctions at the superconducting interfaces but even for electron doping and high Tr we find $\alpha \approx 0.4$ (Fig. 2c). Furthermore, we measured the excess current $I_e > I_c$ as shown in Fig. 2a and found that, in the case of I_e , α also does not reach a value close to 2.1 (Fig. 2c). This corresponds to the fact that all our devices were in the limit of long $L > \Delta/hv_F$ (v_F is the Fermi velocity), as also follows from the $1/L$ dependence found for $I_c R_n$ (Fig. 2d). In this long-junction regime, the critical current is given by $I_c \approx E_{Th}/eR_n$ being determined by the Thouless energy E_{Th} rather than the superconducting gap^{2,17,24}. For a ballistic system, E_{Th} depends on time charge carriers spent inside the FP cavity and can be estimated²⁵ as $\sim hv_F/L$. This yields $I_c \propto 1/L$ and $I_c R_n \propto 1/L$ because R_n is independent of ballistic device's length. Our detailed studies of I_c as a function of T and L show that all data for $I_c R_n/E_{Th}$ collapse on a universal curve $f(T/E_{Th})$ with $E_{Th} \sim hv_F/L$, which again agrees well with expectations for the long-junction limit (Supplementary Section 4). We estimate that to reach the transition regime $E_{Th}/\Delta \sim 1$ for our SGS junctions would require $L < 100$ nm. Let us also mention that no definitive signs of specular Andreev reflection^{3,17} were found in our devices (Supplementary Section 4).

As a consequence of FP resonances in the normal state (Fig. 1), the supercurrent also exhibits quantum oscillations that are clearly seen in Fig. 2b for hole doping. Eq. (1) implies that such oscillations in I_c should occur simply because R_n oscillates. Indeed, R_n and I_c are found to oscillate in antiphase, compensating each other in the final products $I_c e R_n$. However, we find that oscillations in the critical current are approximately 3 times stronger than those in R_n . This observation is consistent with the fact that I_c is not only inverse proportional to R_n but also depends on the Thouless energy as discussed above whereas the latter is expected to oscillate because of the oscillating transparency of FP resonators (Supplementary Section 4).

In magnetic field B , our ballistic junctions exhibit further striking departures from the conventional behavior (Fig. 3). In small B such that a few flux quanta $\phi_0 = h/2e$ enter an SGS junction, we observe the standard Fraunhofer dependence²

$$I_c = I_c(B=0) |\sin(\pi\Phi/\phi_0)/(\pi\Phi/\phi_0)| \quad (2)$$

where $\Phi = L \times W \times B$ is the flux through the junction area. Marked deviations from eq. (2) occur in $B > 5$ mT (Fig. 3a). Figures 3b-e show that, in this regime, the supercurrent no longer follows the oscillatory Fraunhofer pattern but pockets of proximity superconductivity can randomly appear as a function of n and B . At low doping, the pockets can be separated by extended regions of the normal state where no supercurrent could be detected with accuracy of a few nA $\ll I_Q$ (Figs. 3c,e). Within each pocket, I-V characteristics exhibit a gapped behavior (inset of Fig. 3d) with $I_c \sim I_Q \approx 40$ nA, although the exact value depends on doping and I_c falls down to ≈ 10 nA close to the NP, possibly due to rising contributions of electrical noise and thermal fluctuations that suppress apparent I_c (Fig. 3c). These proximity states persist until B as large as ≈ 1 T ($\Phi/\phi_0 \sim 10^3$) and are highly reproducible, although occasional flux jumps in Nb contacts can reset the proximity pattern (Supplementary Section 5). Correlation analysis presented in Supplementary Section 6 yields that, to suppress such superconducting states, it requires changes in Φ of $\approx \phi_0$ and changes in the Fermi energy of ≈ 1 meV.

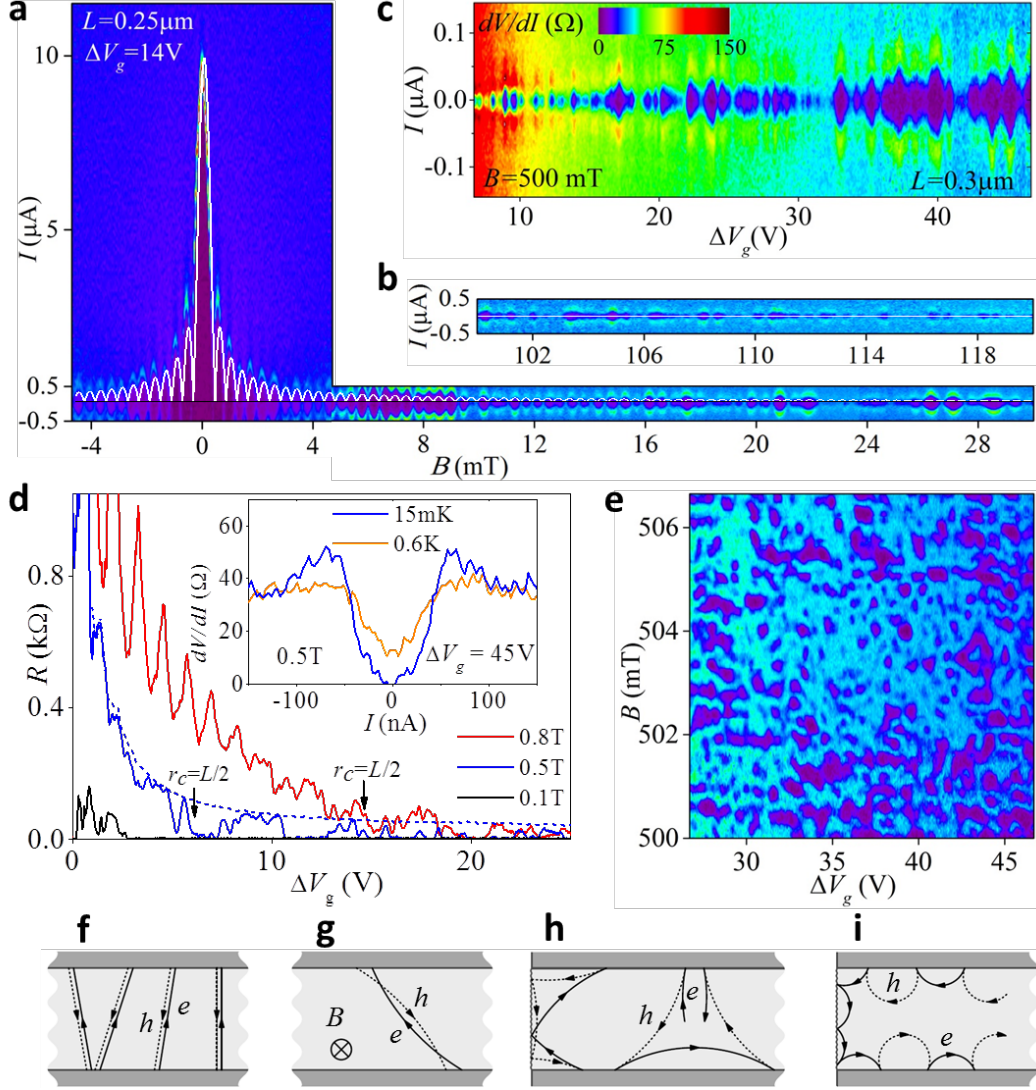


Figure 3] Fluctuating proximity superconductivity. **a**, Example of dV/dI as a function of applied current I and B . The purple regions correspond to the zero-resistance state and their edges mark I_c (see Supplementary Section 10). The map is symmetric in both I and B . The white curve is given by eq. (2). The low- B periodicity is ≈ 0.4 mT, smaller than expected from the device's area, which is attributed to the Meissner screening that focuses the field into the junction³⁰. **b**, Continuation of the map from (a) above 0.1 T. Intervals with finite I_c continue randomly appear, despite the Fraunhofer curve is indistinguishable from zero. **c**, Another high- B example but as a function of ΔV_g in 0.5 T. **d**, Examples of low-current resistance ($I = 2$ nA) in different B . The dashed curve for 0.5 T shows that current $I = 150$ nA $> I_q$ completely suppresses superconductivity. The arrows mark the expected onset of edge state transport. **e**, Local map of fluctuating superconductivity. $T \approx 10$ mK; all color scales are as in (c). Inset in (d): Typical I-V characteristics for high- B superconducting states. **f-i**, Electron-hole paths responsible for Andreev states in ballistic junctions in zero (f), intermediate (g,h) and high B (i). In (h), the cyclotron bending suppresses the transfer of Cooper pairs in the middle of the graphene strip but Andreev states can persist near the edges.

The semiclassical description^{2,24-27} of the superconducting proximity relates the Cooper pair transfer between the leads to electrons and Andreev-reflected holes, which travel along same trajectories but in opposite directions (Fig. 3f). In low B , interference between many Andreev states traversing the graphene strip results in the Fraunhofer-type oscillatory suppression of I_c described by Eq. (2)

(see Fig. 3a). Although not reported before, the Fraunhofer pattern in ballistic devices can be expected to break down in relatively small B because the cyclotron motion deflects electrons and holes in opposite directions so that they can no longer retrace each other (Fig. 3g). We have estimated the field required to suppress Andreev states in the bulk as $B^* \sim \Delta/eLv_F$ (Supplementary Section 7). For the devices in Fig. 3, this yields $B^* \approx 5$ mT, in agreement with the field where strong deviations from the Fraunhofer curve are observed.

As for the random pockets of superconductivity at $B \gg B^*$ which exhibit I_c much higher than that expected from Eq. (2), we invoke the previously noticed analogy¹⁸ between mesoscopic fluctuations in the normal-state conductance²⁸, $\langle \delta G^2 \rangle$ and in the supercurrent^{17,18}, $\langle \delta I_c^2 \rangle$. Both types of fluctuations are due to interference of electron waves propagating along different paths but start and finish together. In contrast to the case of $B = 0$, for which semiclassical phases of counter-propagating electrons and holes near the Fermi level cancel each other because of time-reversal symmetry (Fig. 3f), electrons and holes propagating along non-retracing trajectories in a finite B acquire large and random phase differences (Figs. 3g,h). Averaging over all imaginable geometrical paths would lead to complete suppression of the supercurrent¹⁸. However, for each given realisation of either diffusive or chaotic ballistic SNS junction, the characteristic values of fluctuations are set^{17,18,28-30} at $\langle \delta G^2 \rangle^{1/2} \sim e^2/h$ and $\langle \delta I_c^2 \rangle^{1/2} \sim e\Delta/h$. In the case of $B \gg B^*$, non-retracing paths that can transfer Cooper pairs between superconducting contacts can occur only near graphene edges (see Fig. 3h and Supplementary Section 7). In a way, a combination of cyclotron motion and edge scattering provides a chaotic ballistic billiard near each graphene edge, and this leads to random pockets of superconductivity with $I_c = \langle \delta I_c^2 \rangle^{1/2} \sim I_Q$. Moreover, the analogy with chaotic billiards allows us to estimate the change in the Fermi energy, which is needed to change a realization of the mesoscopic system and, therefore, suppress an existing pocket of superconductivity. The required change is again given by the Thouless energy $E_{Th} \sim \hbar v_F/\Lambda$ where Λ is the typical length of Andreev paths in a strong magnetic field (Fig. 3h). At high B , we estimate Λ as $\approx (r_c L)^{1/2}$ where r_c is the cyclotron radius. This yields $E_{Th} \leq 1$ meV, in agreement with the observed changes in doping which are required to suppress the pockets of superconducting proximity (Supplementary Section 6). An interference pattern in mesoscopic systems is also known^{18,28-30} to change upon changing the flux Φ through the system by $\approx \phi_0$. This scale agrees well with that observed experimentally (Fig. S8).

Finally, the discussed mesoscopic proximity effect can be expected to disappear if r_c becomes shorter than $L/2$ (Fig. 3i). This condition is marked in Fig. 3d and seen more clearly in the data of Supplementary Section 8. It is also worth noting that the near-edge superconductivity was not observed for hole doping, which we attribute to the fact that Klein tunneling in graphene collimates trajectories perpendicular to the pn interface²³, making it essentially impossible to form closed-loop Andreev states shown in Fig. 3h (Supplementary Section 7). In principle, the effect of near-edge Andreev states could be further enhanced by presence of extended electronic states at graphene edges¹⁶ but, based on our experimental data, no evidence for this or other spatial inhomogeneity was found in the studied samples (Supplementary Section 9).

Methods

The measurements were carried out in a helium-3 cryostat for T down to 0.3 K and in a dilution refrigerator, for lower T . All electrical connections to the sample passed through cold RC filters

(Aivon Therma) and additional ac filters were on the top of the cryostats. The differential resistance was measured in the quasi-four-terminal geometry (using 4 superconducting leads to an SGS junction) and in the current-driven configuration using an Aivon preamplifier and a lock-in amplifier. To probe the superconducting proximity, we used an excitation current of 2 nA.

References

- [1] H. Meissner. Range of order of superconducting electrons. *Phys. Rev. Lett.* **2**, 458-459 (1959).
- [2] M. Tinkham, *Introduction to superconductivity*. Courier Dover Publications, 2012.
- [3] C. W. J. Beenakker. Colloquium: Andreev reflection and Klein tunneling in graphene. *Rev. Mod. Phys.* **80**, 1337-1354 (2008).
- [4] H. B. Heersche, P. Jarillo-Herrero, J. B. Oostinga, L. M. K. Vandersypen, A. F. Morpurgo. Bipolar supercurrent in graphene. *Nature* **446**, 56-59 (2007).
- [5] F. Miao, S. Wijeratne, Y. Zhang, U. C. Coskun, W. Bao, C. N. Lau. Phase-coherent transport in graphene quantum billiards. *Science* **317**, 1530-1533 (2007).
- [6] X. Du, I. Skachko, E. Andrei. Josephson current and multiple Andreev reflections in graphene SNS junctions. *Phys. Rev. B* **77**, 184507 (2008).
- [7] C. Ojeda-Aristizabal, M. Ferrier, S. Guéron, H. Bouchiat. Tuning the proximity effect in a superconductor-graphene-superconductor junction. *Phys. Rev. B* **79**, 165436 (2009).
- [8] C. Girit *et al.* Tunable graphene dc superconducting quantum interference device. *Nano Lett.* **9**, 198–199 (2009).
- [9] I. V. Borzenets, U. C. Coskun, S. J. Jones, G. Finkelstein. Phase diffusion in graphene-based Josephson junctions. *Phys. Rev. Lett.* **107**, 137005 (2011).
- [10] K. Komatsu, C. Li, S. Autier-Laurent, H. Bouchiat, S. Gueron. Superconducting proximity effect through graphene from zero field to the quantum Hall regime. *Phys. Rev. B* **86**, 115412 (2012).
- [11] U. C. Coskun, M. Brenner, T. Hymel, V. Vakaryuk, A. Levchenko, A. Bezryadin. Distribution of supercurrent switching in graphene under proximity effect. *Phys. Rev. Lett.* **108**, 097003 (2012).
- [12] N. Mizuno, B. Nielsen, X. Du. Ballistic-like supercurrent in suspended graphene Josephson weak links. *Nature Commun.* **4**, 3716 (2013).
- [13] J. H. Choi *et al.* Complete gate control of supercurrent in graphene pn junctions. *Nature Commun.* **4**, 3525 (2013).
- [14] F. Deon, S. Šopić, A. F. Morpurgo. Tuning the influence of microscopic decoherence on the superconducting proximity effect in a graphene Andreev interferometer. *Phys. Rev. Lett.* **112**, 126803 (2014).
- [15] V. E. Calado *et al.* Ballistic Josephson junctions in edge-contacted graphene. arXiv:1501.06817.
- [16] M. T. Allen *et al.* Spatially resolved edge currents and guided-wave electronic states in graphene. arXiv:1504.07630.
- [17] C. W. J. Beenakker. Universal limit of critical-current fluctuations in mesoscopic Josephson junctions. *Phys. Rev. Lett.* **67**, 3836-3839 (1991).
- [18] B. L. Altshuler, B. Z. Spivak. Mesoscopic fluctuations in a superconductor-normal metal-superconductor junction. *Sov. Phys. JETP* **65**, 343-347 (1987).
- [19] A. S. Mayorov *et al.* Micrometer-scale ballistic transport in encapsulated graphene at room temperature. *Nano Lett.* **11**, 2396-2399 (2011).
- [20] L. Wang *et al.* One-dimensional electrical contact to a two-dimensional material. *Science* **342**, 614-617 (2013).
- [21] I. P. Krylov, Y. V. Sharvin. Radio-frequency size effect in a layer of normal metal bounded by its superconducting phase. *Sov. Phys. JETP* **37**, 481-486 (1973).
- [22] P. Blake *et al.* Influence of metal contacts and charge inhomogeneity on transport properties of graphene near the neutrality point. *Solid State Commun.* **149**, 1068-1071 (2009).
- [23] P. Rickhaus *et al.* Ballistic interferences in suspended graphene. *Nature Commun.* **4**, 2342 (2013).

- [24] P. Dubos, H. Courtois, B. Pannetier, F. K. Wilhelm, A. D. Zaikin, G. Schön. Josephson critical current in a long mesoscopic SNS junction. *Phys. Rev. B* **63**, 064502 (2001).
- [25] C. Ishii. Josephson currents through junctions with normal metal barriers. *Prog. Theor. Phys.* **44**, 1525-1547 (1970).
- [26] A. F. Andreev. The thermal conductivity of the intermediate state in superconductors. *Sov. Phys. JETP* **19**, 1228-1231 (1964).
- [27] T. M. Klapwijk. Proximity effect from an Andreev perspective. *J. Superconductivity* **17**, 593-611 (2004).
- [28] R. A. Jalabert, H. U. Baranger, A. D. Stone. Conductance fluctuations in the ballistic regime: A probe of quantum chaos? *Phys. Rev. Lett.* **65**, 2442-2445 (1990).
- [29] H. Takayanagi, J. B. Hansen, J. Nitta. Mesoscopic fluctuations of the critical current in a superconductor—normal-conductor—superconductor. *Phys. Rev. Lett.* **74**, 166-169 (1995).
- [30] J. P. Heida, B. J. van Wees, T. M. Klapwijk, G. Borghs. Nonlocal supercurrent in mesoscopic Josephson junctions. *Phys. Rev. B* **57**, 5618-5621 (1998).